Fast-ion losses induced by ELMs and externally applied magnetic perturbations in the ASDEX Upgrade tokamak

2013 Plasma Phys. Control. Fusion 55 124014

(http://iopscience.iop.org/0741-3335/55/12/124014)

Plasma Phys. Control. Fusion **55** (2013) 124014 (12pp) doi:10.1088/0741-3335/55/12/124014

Fast-ion losses induced by ELMs and externally applied magnetic perturbations in the ASDEX Upgrade tokamak

M Garcia-Munoz[1], S Äkäslompolo[2], P de Marne[3], M G Dunne[3,4], R Dux[3], T E Evans[5], N M Ferraro[5], S Fietz[3], C Fuchs[3], B Geiger[3], A Herrmann[3], M Hoelzl[3], B Kurzan[3], N Lazanyi[6], R M McDermott[3], M Nocente[7,8], D C Pace[5], M Rodriguez-Ramos[1], K Shinohara[9], E Strumberger[3], W Suttrop[3], M A Van Zeeland[5], E Viezzer[3], M Willensdorfer[10], E Wolfrum[3] and the ASDEX Upgrade Team

[1] FAMN Department, Faculty of Physics, University of Seville, 41012 Seville, Spain
[2] School of Science, Aalto University, PO Box 14100, FI-00076 AALTO, Finland
[3] Max-Planck-Institut für Plasmaphysik, EURATOM Association, D-85748, Germany
[4] Department of Physics, University College Cork, Association Euratom-DCU, Cork, Ireland
[5] General Atomics, San Diego, CA, 92186-5608, USA
[6] BME NTI, Association EURATOM, Pf 91, H-1521 Budapest, Hungary
[7] Dipartimento di Fisica 'G. Occhialini', Universita degli Studi di Milano-Bicocca, Piazza della Scienza 3, 20126, Milano, Italy
[8] Istituto di Fisica del Plasma Piero Caldirola-CNR, Milano, Italy
[9] JAEA, 801-1, Mukouyama, Naka City, Ibaraki, 311-0193, Japan
[10] Technische Universität Wien, Association EURATOM-ÖAW, Vienna, Austria

E-mail: Manuel.Garcia-Munoz@ipp.mpg.de

Received 5 July 2013, in final form 1 October 2013
Published 28 November 2013
Online at stacks.iop.org/PPCF/55/124014

Abstract

Phase-space time-resolved measurements of fast-ion losses induced by edge localized modes (ELMs) and ELM mitigation coils have been obtained in the ASDEX Upgrade tokamak by means of multiple fast-ion loss detectors (FILDs). Filament-like bursts of fast-ion losses are measured during ELMs by several FILDs at different toroidal and poloidal positions. Externally applied magnetic perturbations (MPs) have little effect on plasma profiles, including fast-ions, in high collisionality plasmas with mitigated ELMs. A strong impact on plasma density, rotation and fast-ions is observed, however, in low density/collisionality and q_{95} plasmas with externally applied MPs. During the mitigation/suppression of type-I ELMs by externally applied MPs, the large fast-ion bursts observed during ELMs are replaced by a steady loss of fast-ions with a broad-band frequency and an amplitude of up to an order of magnitude higher than the neutral beam injection (NBI) prompt loss signal without MPs. Multiple FILD measurements at different positions, indicate that the fast-ion losses due to static 3D fields are localized on certain parts of the first wall rather than being toroidally/poloidally homogeneously distributed. Measured fast-ion losses show a broad energy and pitch-angle range and are typically on banana orbits that explore the entire pedestal/scrape-off-layer (SOL). Infra-red measurements are used to estimate the heat load associated with the MP-induced fast-ion losses. The heat load on the FILD detector head and surrounding wall can be up to six times higher with MPs than without 3D fields. When 3D fields are applied and density pump-out is observed, an enhancement of the fast-ion content in the plasma is typically measured by fast-ion D-alpha (FIDA) spectroscopy. The lower density during the MP phase also leads to a deeper beam deposition with an inward radial displacement of ≈2 cm in the maximum of the beam emission. Orbit simulations are used to test different models for 3D field equilibrium reconstruction including vacuum representation, the free boundary NEMEC code and the two-fluid M3D-C1 code which account for the plasma response. Guiding center simulations predict the maximum level of losses, ≈2.6%, with NEMEC 3D equilibrium. Full orbit simulations overestimate the level of losses in 3D vacuum fields with ≈15% of lost NBI ions.

(Some figures may appear in colour only in the online journal)

1. Introduction

Edge localized modes (ELMs) are inherent to high confinement regimes in tokamak plasmas. The energy and particle release associated with the ELM crash are likely be intolerable in future fusion devices such as ITER; therefore, several mitigation techniques have been developed during the last years. Among others, externally applied magnetic perturbations (MPs) are one of the most promising techniques [1–4]. However, the impact that the externally applied MPs have on energetic particles still needs to be assessed experimentally. This is of special importance for future burning plasmas with a large content of MeV-ions with relatively long slowing-down times. Numerical simulations of fast-ion losses induced by ELM mitigation coils in ITER [5–9] have shown that, under certain conditions, up to 20% of the neutral beam injection (NBI) power can be lost due to the 3D fields created by the ELM mitigation coils. An experimentally validated model for the plasma response is, however, needed to improve our abilities to make realistic predictions for ITER as the plasma can shield or even amplify some components of the externally applied MPs leading to a complex 3D background equilibrium.

In this paper, the first measurements of fast-ion losses induced by ELMs and ELM mitigation coils in H-mode plasmas are presented. The experiments discussed here have been carried out in a rather low collisionality ($\nu_e^* \leqslant 1$), density ($\bar{n}_e \leqslant 6.5 \times 10^{19}\,\mathrm{m}^{-2}$) and q_{95} ($\leqslant$3.85) plasma with static $n = 2$ MPs applied by the 16 ELM mitigation coils that have been recently installed in the ASDEX Upgrade (AUG) tokamak [4]. The fast-ion losses are measured by two scintillator based fast-ion loss detectors (FILDs) [10], located at different toroidal positions but at the same poloidal position (≈30 cm above the mid-plane). The MHz bandwidth of the detectors allows a high temporal resolution of the intra-ELM fast-ion losses. Indeed, several fast-ion filaments are typically observed almost simultaneously within a single ELM by both FILD systems. Externally applied MPs have little effect on plasma profiles, including fast-ions, in high collisionality plasmas with mitigated ELMs. A strong impact on the plasma rotation, density (with a pump-out of up to 25% of the core line integrated density) and fast-ion population is observed, however, in low-collisionality and low-q_{95} plasmas with externally applied MPs and partially mitigated ELMs. Orbit simulations are used to test different models for 3D field equilibrium reconstruction, including the vacuum representation, the free boundary NEMEC code [11, 12] and the two-fluid M3D-C1 code [13, 14]. In order to account for modifications of the NBI prompt loss pattern due to perturbed density profiles with density pump-out, the perturbed NBI birth distribution has been calculated using the F90FIDASIM code [15] with measured density profiles with and without MPs. The deeper beam deposition achieved during the MP phase due to the lower density indicates that the perturbation fields are likely affecting fast-ions that would be well confined in an unperturbed equilibrium.

This paper is organized as follows. In section 2 the experimental observations including the response to the 3D fields of the background plasma and of the fast-ions are described in detail. The modeling strategy is presented in section 3, with emphasis on the perturbed NBI birth distributions and 3D fields. Finally, some conclusions are given in section 4.

2. Experimental observation

The experiments presented here have been carried out in H-mode plasmas with a toroidal magnetic field, $B_t = -1.7$ T; a plasma current, $I_P = 0.8$ MA; 1.4 MW of ECRH to avoid impurity accumulation; 5 MW of NBI heating as main fast-ion source; and an externally applied $n = 2$ static MP. The current of the coils was set to $I_{coil} \approx 1.2$ kA·t. The discharge is divided in three phases that have been heated with three different beams (with different injection geometries) to vary the dominant pitch-angle of the fast-ions in the plasma as well as the plasma rotation, i.e. possible plasma shielding. All three NBI phases have a 500 ms phase with the ELM mitigation coils ON. The NBI#3 source was kept ON during the entire discharge for diagnostic purposes. Figure 1 shows the injection geometry of the beams used in these experiments together with the coils geometry and the location of the FILD detectors.

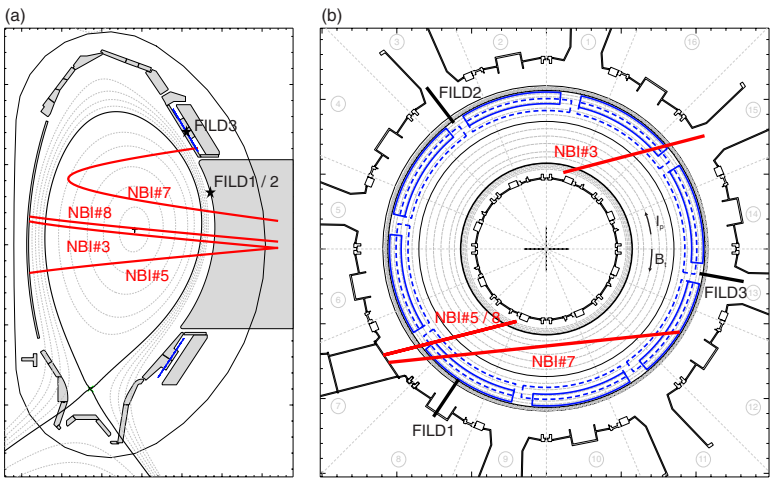

Figure 1. Beam injection (red) and B-coils geometry (blue). (*a*) Poloidal cross section. (*b*) Toroidal cross section. The location of the three FILD systems is marked with black stars and solid lines in the poloidal and toroidal cross sections respectively.

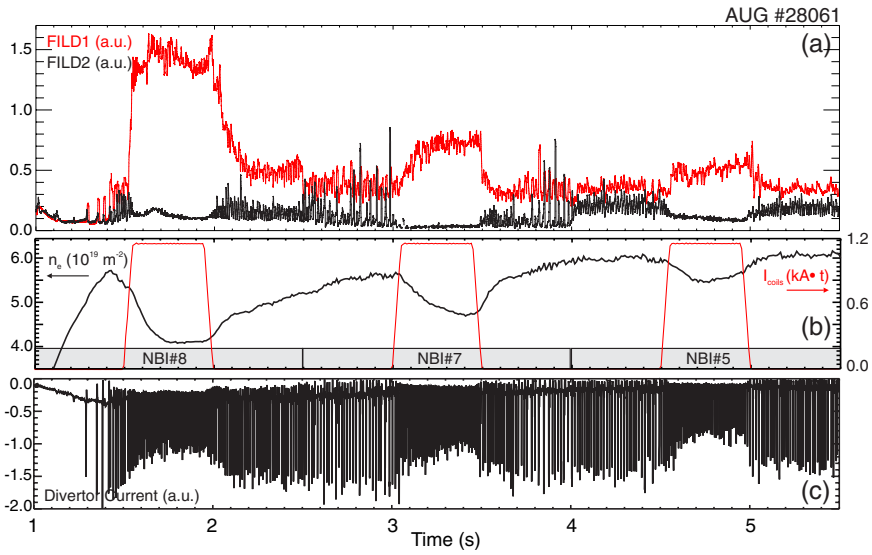

Figure 2. AUG discharge #28061. Overview of most relevant signals. (*a*) Time trace of FILD1 and FILD2 signals integrated in velocity-space. (*b*) Temporal evolution of the core line integrated signal. (*c*) ELM monitor, divertor current.

2.1. Measurements of fast-ion losses due to ELMs and externally applied MPs

An overview of the most relevant signals is shown in figure 2. The time traces of the whole fast-ion losses (integrated in velocity-space) measured by the FILD1 and FILD2 CCD cameras are shown in figure 2(*a*).

The strongest losses appear in FILD1 and are clearly correlated with the application of the $n = 2$ MP during the first NBI phase. There are striking differences in the overall evolution of FILD1 and FILD2 signals with MP-induced fast-ion losses concentrated in FILD1 signals. While FILD1 signals rise dramatically with the external MPs, the fast-ion losses on FILD2 seem to vanish. FILD1 signals exhibit two clear characteristic times in the temporal response to the ELM mitigation coils as the rise and decay time of the losses are quite different in all three coil phases but most pronounced in the first coil phase. ELM-induced fast-ion losses are visible in both detectors, though this is more evident with the faster sampled signal presented in figure 3. The temporal evolution of the core line integrated density is shown in figure 2(*b*), together with the timing of the NBI scan. Density pump-out is observed in all MP phases with a clear density/collisionality dependence, i.e. as the discharge evolves, the density rises and so the density pump-out become smaller. The same behavior is observed in FILD1 signals, i.e. the lower the density, the larger the density pump-out and the stronger the fast-ion losses measured in FILD1. The discharge exhibits a marginal ELM mitigation with the externally applied MPs that becomes more significant as the plasma density increases in time; see figure 2(*c*). Figure 3(*a*) shows a zoom of the fast-ion losses measured with FILD1 PMTs during the first MP phase of the discharge. Before the coils are switched ON at $t = 1.5$ s, FILD1 is measuring only bursting ELM-induced fast-ion losses on top of a dc signal that corresponds to the level of NBI prompt losses. The fast-ion losses induced by two ELMs and measured by both FILDs are expanded in figure 3(*b*). In analogy to the well-known filaments of thermal plasma observed routinely during ELMs [16], fast-ion filaments are referred to here as individual intra-ELM fast-ion bursts with characteristic time-scales that are observed simultaneously by several detectors at different toroidal positions, indicating their extension along field lines. At $t = 1.5$ s, the coils are ramped up and the dc component of the fast-ion losses rises quickly up to a level that is ≈7–8 times the NBI prompt loss level without the external perturbation. During the MP phase, the mitigated ELMs (smaller and more frequent) have a completely different impact on the fast-ion loss signal, i.e. instead of causing filamentary fast-ion losses, the remaining ELMs are causing a drop in the fast-ion loss signal, as shown in figure 3(*c*). After the coils are switched off at $t = 2.0$ s, the FILD1 signals decay slowly with a characteristic time much longer (a few times the fast-ion slowing-down time) than the rise time observed during the coil ramp up. Indeed, as the coils are switched on, the maximum in FILD signals is achieved within 10 ms while FILD signals are back to the nominal prompt loss level after switching off the coils in ≈200 ms. The heat loads caused by the externally applied MPs on FILD1 and the surrounding first wall area has been measured with a fast-sampling infra-red camera; see figure 4. If we compare the time trace of the heat loads, figure 4(*a*), with the time traces of figure 2, it becomes evident that the stronger the plasma response is, i.e. the larger the density pump out, the stronger the fast-ion response is and thus the measured heat loads on the FILD1 detector head. The heat loads on FILD are the largest during the first MP phase and decrease during the other MP phases as the plasma density rises. Figures 4(*b*) and (*c*) show 2D images of the heat loads and the temperature of the FILD1 detector head. The velocity-space of the escaping NBI ions measured by FILD identifies unequivocally the orbits of the ions that are most affected by the perturbation fields. In figure 5, the gyroradii (energies) and pitch-angles of the escaping ions measured by FILD1 with and without the MP coils during the different NBI phases are shown. Figure 5(*a*), coils off, and (*b*), coils on, correspond to the NBI#3 + #8 phase. Figure 5(*c*), coils off,

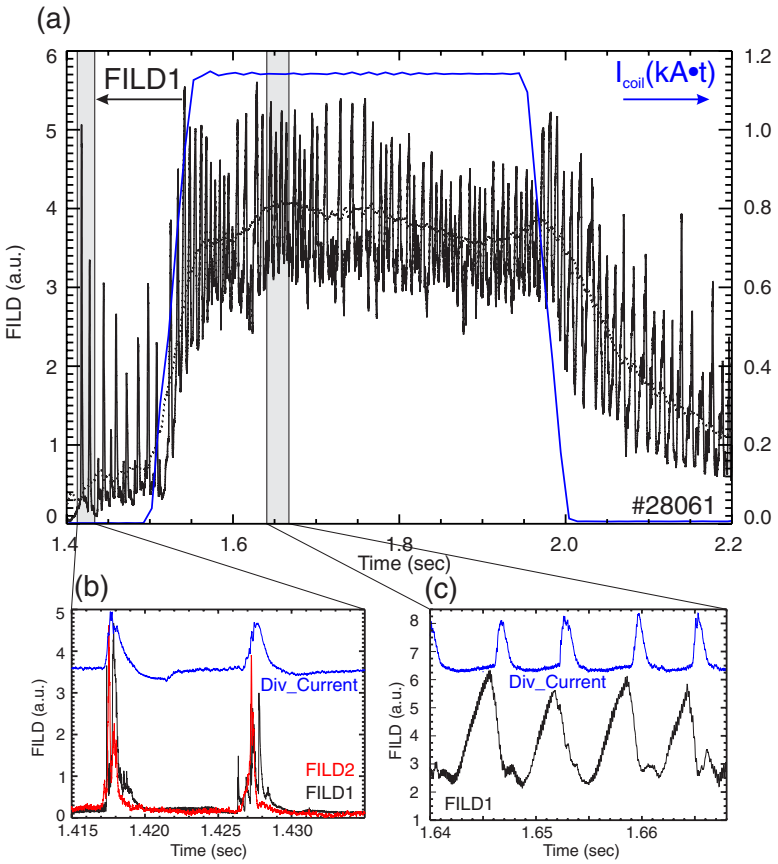

Figure 3. AUG discharge #28061. Detail of fast-ion losses during MP phase. (*a*) FILD1 signal during the entire MP phase. (*b*) ELM-induced fast-ion losses measured by FILD1 and FILD2. (*c*) Effect of ELMs on MP-induced fast-ion losses measured by FILD1.

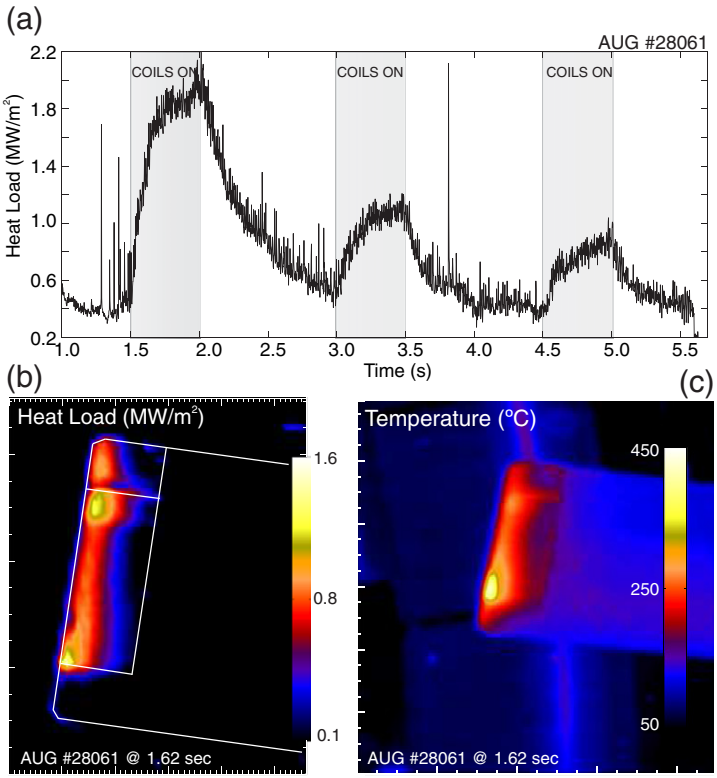

Figure 4. AUG discharge #28061. (*a*) Time trace of heat load on detector aperture. (*b*) 2D image of heat load due to ELM mitigation coils on FILD detector head. (*c*) 2D image of detector head temperature.

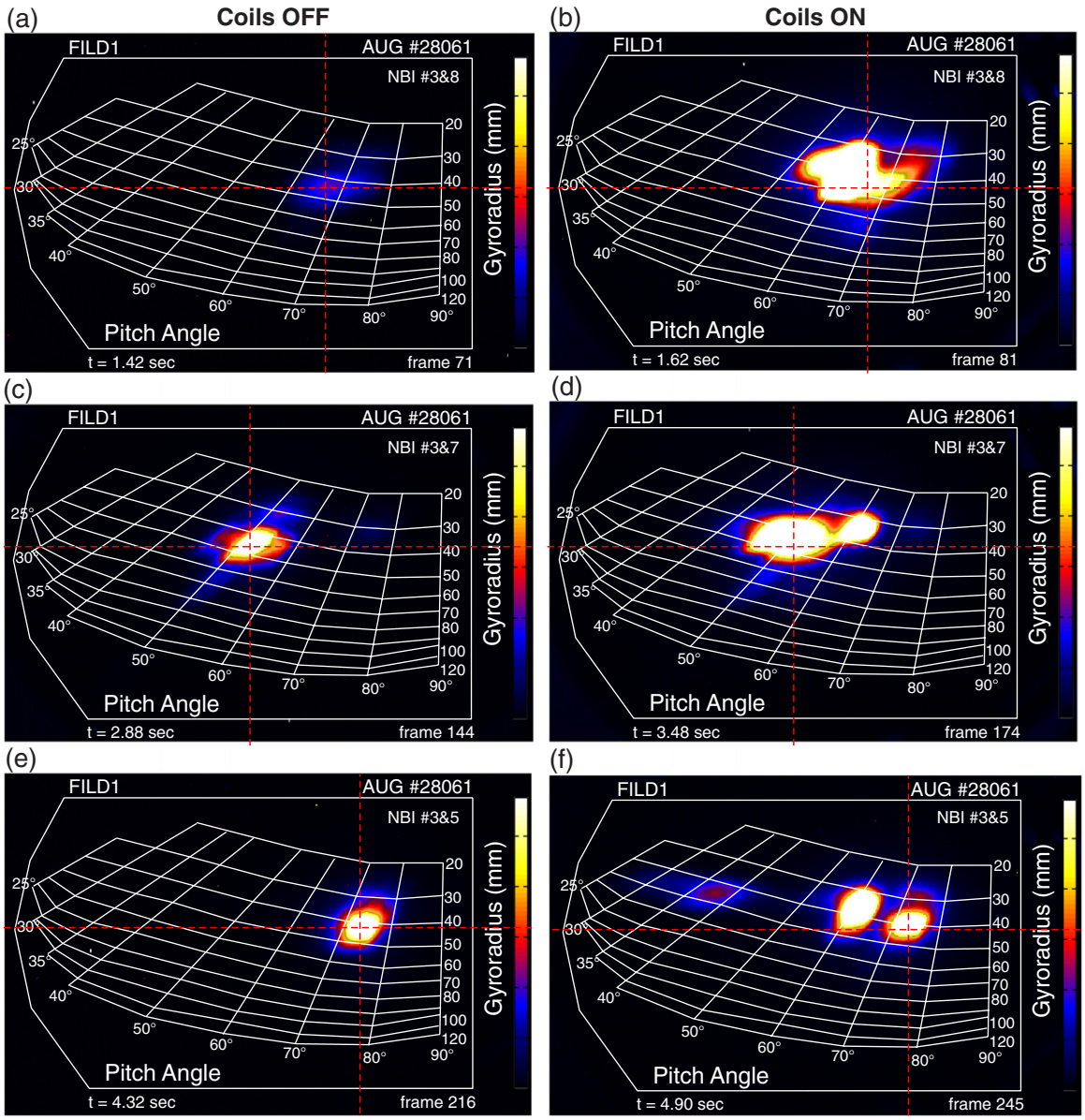

Figure 5. AUG discharge #28061. Velocity-space of escaping ions measured by FILD1 with MP coils OFF, (*a*), (*c*) and (*e*) and with MP coils on, (*b*), (*d*) and (*f*).

and (*d*), coils on, correspond to the NBI#3 + #7 phase and figure 5(*e*), coils off, and (*f*), coils on, to the NBI#3+#5 phase. Figures 5(*a*), (*c*) and (*e*) give an overview of the NBI prompt losses, with ≈93 keV, measured by FILD1. The intensity, energy and pitch-angle of the NBI prompt losses measured by FILD systems depend mainly on the density profile, the beam injection geometry and the magnetic field configuration, as prompt losses are, per definition, lost particles that are initially born on open trajectories (not closed poloidally) that are connected directly with the wall or, in this case, with the FILD detectors. The different intensities of figures 5(*a*), (*c*) and (*e*) indicate that either the corresponding NBI source deposits fewer particles on open trajectories or that they hit the wall at different positions, i.e. the prompt loss open trajectories are not connected to the FILD detectors. The different pitch-angles of the measured NBI prompt losses are a direct measure of the NBI injection geometry, and so radial beams (figures 5(*a*) and (*e*)) cause prompt loss with larger pitch-angles than tangential beams (figure 5(*c*)). In addition to the NBI prompt losses, figures 5(*b*), (*d*) and (*f*) show the new velocity-space areas covered with fast-ion losses due to the MP coils. In all cases, fast-ion losses with gyroradii ≈30–40 mm and pitch-angles ≈60° appear only when the MP coils are on. Figures 5(*b*) and (*d*) show, in addition, other energies and pitch-angles that without the MPs would be well confined. According to the FILD2 time traces shown in figure 2(*a*), the CCD frames of FILD2 show the velocity-space of the NBI prompt losses together with the bursting ELM-induced fast-ion losses before the coils are switched on. However, as soon as the coils are switched on, all signals in FILD2 disappear. Similarly to figure 5, figure 6 shows the velocity-space of the fast-ion losses measured by FILD2 during the three NBI phases.

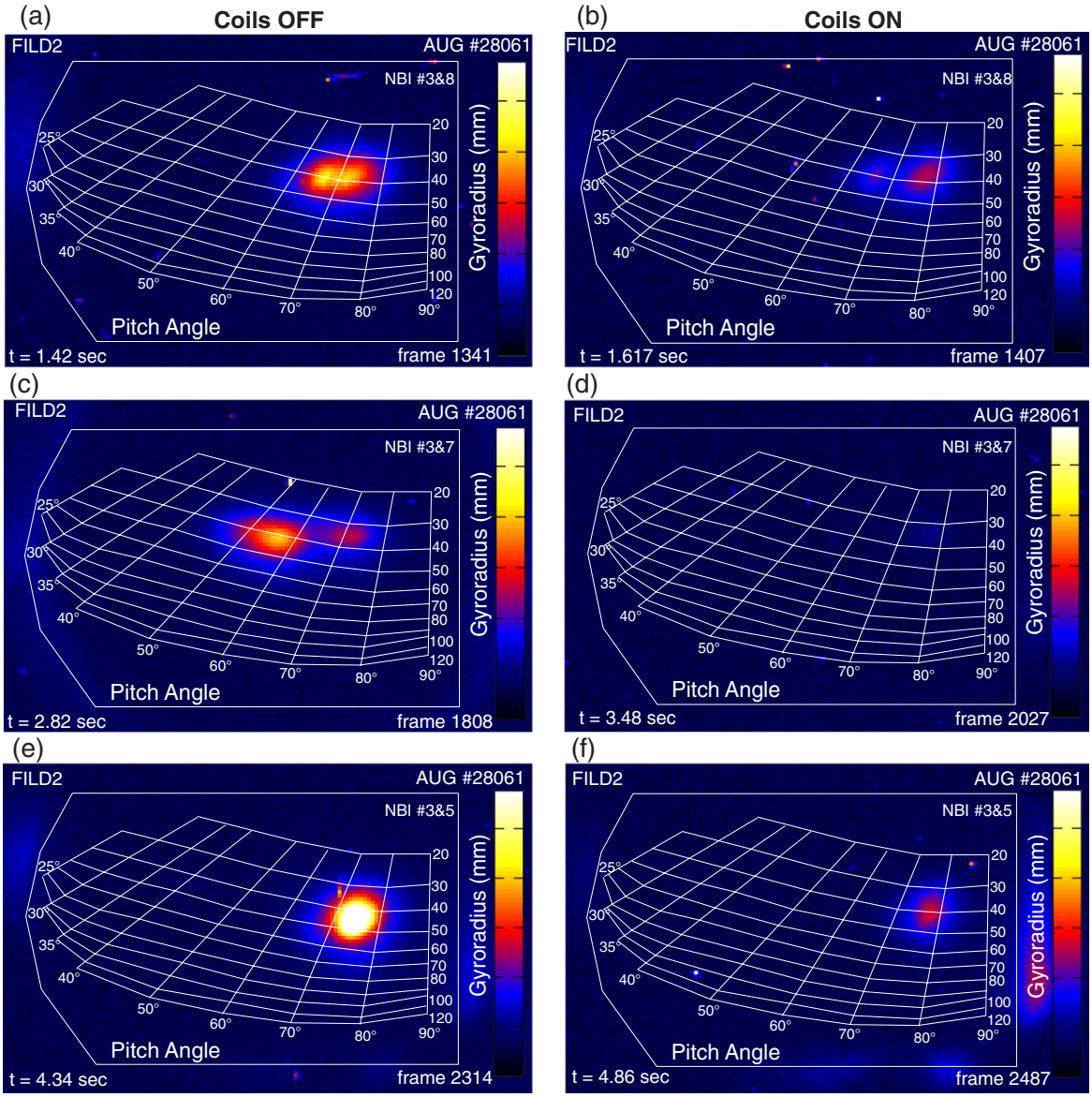

Figure 6. AUG discharge #28061. Velocity-space of escaping ions measured by FILD2 with MP coils on, (*a*), (*c*) and (*e*) and with MP coils on, (*b*), (*d*) and (*f*).

2.2. Plasma response to applied MPs

In order to properly model the perturbed NBI deposition profile and perturbation fields, accurate measurements of the kinetic profiles (density, temperature and rotation) are necessary. The dynamics of the plasma response to the applied MPs have been studied using the AUG comprehensive suite of plasma diagnostics (located at different positions) that includes Thomson scattering (TS), lithium beam, DCN and charge-exchange recombination spectroscopy (CXRS) [17]. While a strong density pump-out is observed in all three MP phases, the electron and ion temperatures, T_e and T_i, are weakly affected. Figure 7 shows the temporal evolution of the electron density and temperature profiles measured by the TS diagnostic during two MP phases. The effect of the density pump-out is also clearly visible in the beam emission spectroscopy (BES) signal, as shown in figure 8. The lower density during the MP phase also leads to a deeper beam deposition with an inward radial displacement of $\approx$ 2 cm in the maximum of the BES emission.

The temporal evolution of the confined fast-ion profiles has been monitored with tangential and vertical active FIDA diagnostics. The FIDA technique is based on the strongly Doppler shifted Balmer alpha radiation ($\lambda = 656.1$ nm, $n = 3 \rightarrow 2$) that fast-ions emit once they charge-exchange with neutrals of a beam as they pass through the beam footprint. Making use of several lines of sight along the beam line, accurate fast-ion profiles can be resolved with ms temporal resolution. As the spectra covered by the tangential FIDA diagnostic includes the beam emission, which originates from the injected deuterium neutrals that get excited as they move through the plasma and decay emitting D-alpha radiation, one can infer a direct measure of the fast-ion content accounting for changes in beam deposition due to density pump-out [15]. Figure 9 shows the temporal evolution of the FIDA emission (*a*), beam emission (same as in figure 8 but with fewer edge

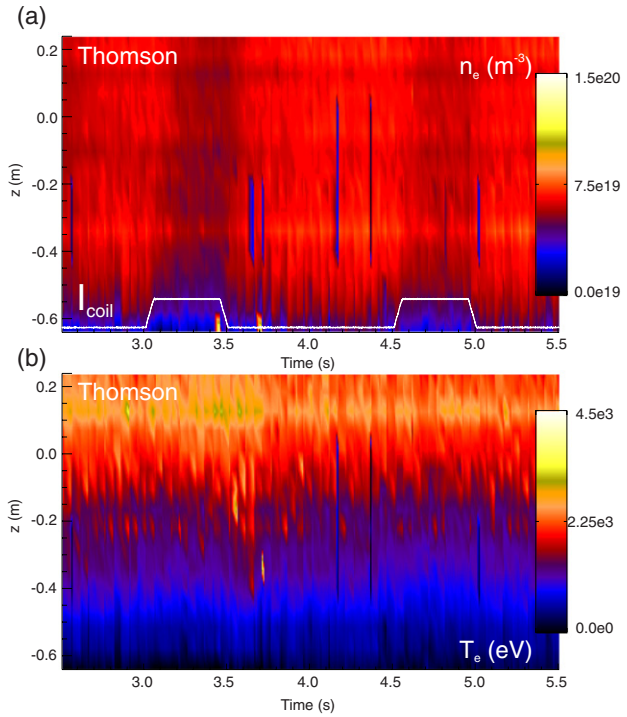

Figure 7. AUG discharge #28061. Temporal evolution of T_e and n_e profiles measured by TS with and without MPs.

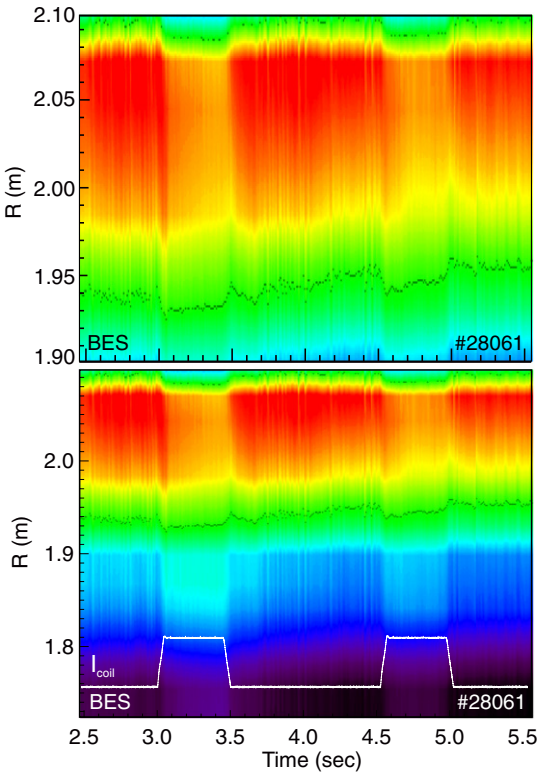

Figure 8. AUG discharge #28061. Beam emission measured with the AUG BES diagnostic. The lower panel shows the beam emission along the entire plasma radius (from the plasma center to the edge) while the upper panel shows only the edge region.

channels) (*b*), and fast-ion density (*c*), profiles. A clear enhancement of the FIDA emission is visible when the MP coils are ON in both NBI phases. In fact, this enhancement of the FIDA emission is due to the larger content of confined

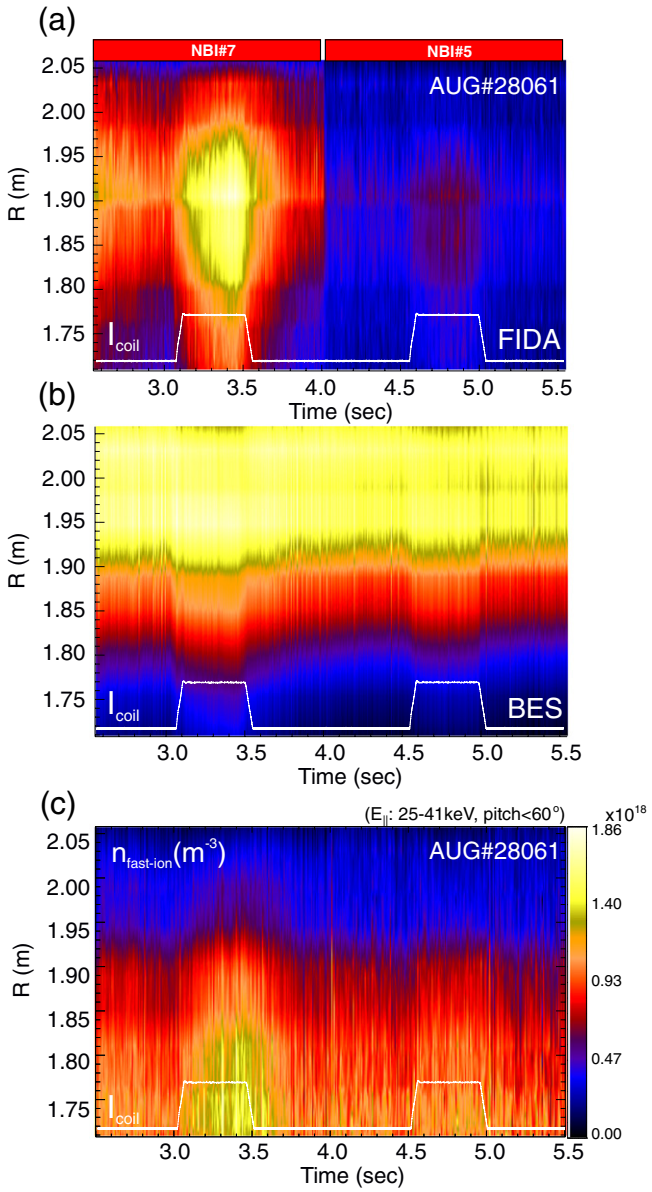

Figure 9. AUG discharge #28061. FIDA diagnostic. (*a*) FIDA emission, (*b*) beam emission (BES) and (*c*) fast-ion density (FIDA/BES).

fast-ions during the MP phase and not only due to a deeper deposition of NBI neutrals as figure 9(*c*) shows with $n_{\text{fast-ion}}$. The lower collisionality due to density pump-out could account for the larger fast-ion content observed during the MP phases.

3. Modeling

The modeling activities carried out here are focused on the two time points presented in figures 5(*a*) and (*b*). To properly model the fast-ion losses induced by externally applied MPs, realistic NBI birth profiles and 3D perturbation fields need to be taken into account.

3.1. Perturbed NBI birth profiles

As we have seen in the previous section, e.g. figure 8, the NBI deposition can be severely affected by the ELM mitigation

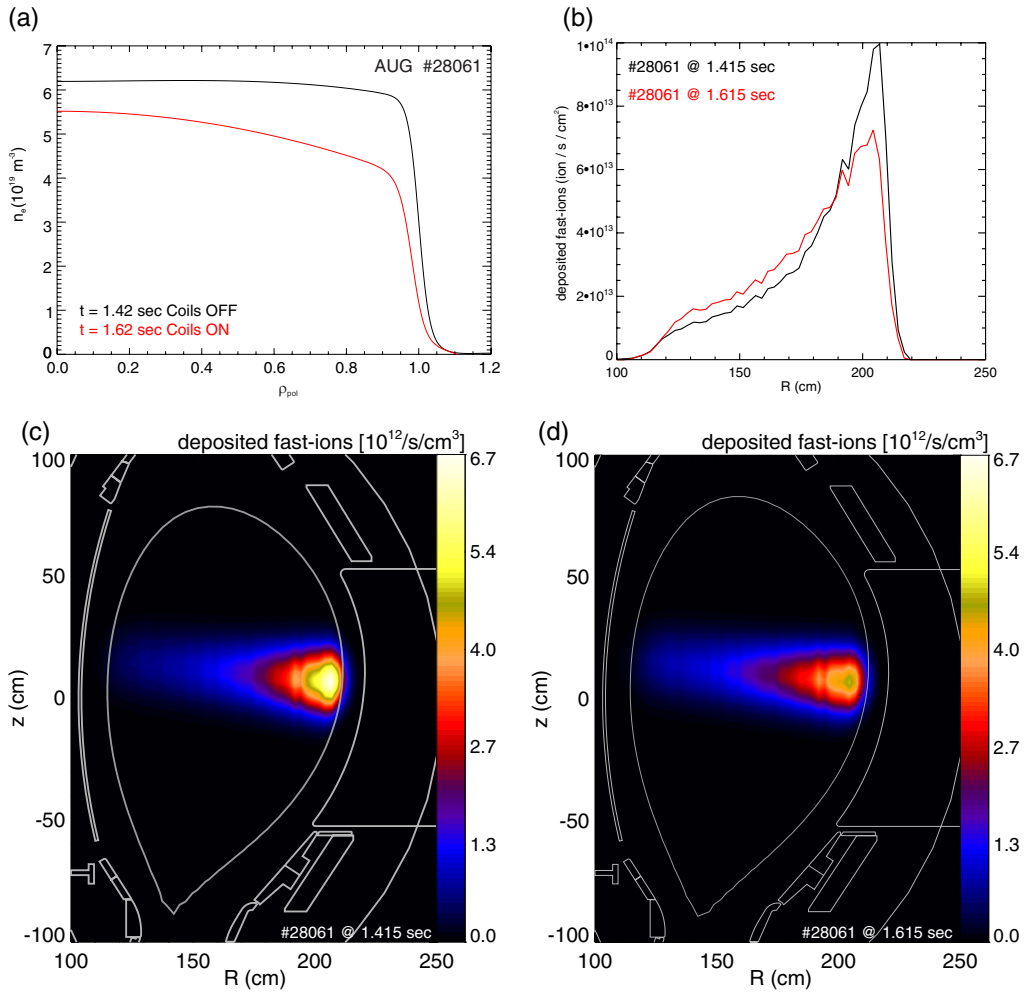

Figure 10. F90FIDASIM simulation of the birth density for the two time points analyzed here with measured kinetic profiles: (*a*) density profiles; (*b*) radial birth density; (*c*) and (*d*) R–z image of the simulated birth density.

coils, thus realistic simulations need to consider NBI birth profiles calculated in perturbed kinetic profiles. This has been done using the F90FIDASIM code for the two time points (with and without MPs) analyzed here, $t = 1.42$ s and $t = 1.61$ s. The measured electron density profiles, n_e, perturbed and unperturbed, used to calculate the density of NBI deposited ions, are shown in figure 10(*a*). A 1D density of the resulting NBI deposited ions can be seen in figure 10(*b*) as a function of the major radius, R. As expected from the BES measurements, the higher density at the edge in the unperturbed phase leads to a higher NBI birth density at the edge, while during the perturbed phase, the NBI birth density is lower at the edge and higher in the core. Figures 10(*c*) and (*d*) show the 2D density of deposited fast-ions on a R–z plane. Intuitively, the higher NBI birth density at the edge at $t = 1.42$ s should lead to stronger losses than the NBI birth density at $t = 1.61$ s. However, stronger losses are observed at $t = 1.61$ s due to the applied 3D fields. The NBI birth profiles calculated here are used as input to the orbit codes GOURDON and ASCOT.

3.2. Reconstruction of 3D fields

The perturbed 3D fields are calculated using the vacuum field representation, the free boundary NEMEC code [11, 12] and the resistive two-fluid M3D-C1 code that calculates the zero-frequency linear plasma response to the applied 3D fields. NEMEC calculates the corrugation of flux surfaces due to the 3D fields assuming nested flux surfaces and including toroidal field (TF) ripple. Figure 11 shows a 3D (*a*) and a 2D (*b*) contour of the corrugation of the flux surfaces at $\Psi_N \approx 99.95\%$ calculated with the NEMEC code for this discharge at $t = 1.61$ s. A maximum displacement of field lines of ± 1.5 cm with respect to the unperturbed equilibrium is clearly visible in both 2D and 3D visualizations. The location of both detectors (indicated in figure 11(*b*)) coincide with a region of minimum field-line displacement. NEMEC predicts a second corrugation maximum of ± 0.5 cm in the plasma core at $q = 1$, as shown in figure 12. In contrast to this, the two-fluid model in M3D-C1 predicts an efficient shielding in the plasma core, though resonant field amplification at rational surfaces with negligible electron rotation causes a stochastic layer in the pedestal due to island overlap. In these calculations, the last closed flux surface is treated as a free boundary, and both the plasma and vacuum regions are treated self-consistently as resistive plasmas. The resistivity profile in each region is taken to be the Spitzer resistivity, calculated using the experimental electron temperature profiles. The two-fluid model

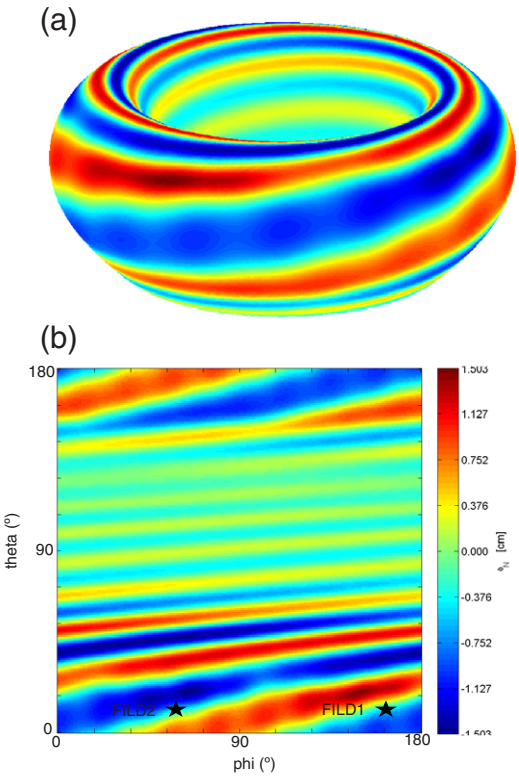

Figure 11. NEMEC simulations of the corrugation of the flux surfaces at $\Psi_N \approx 99.95\%\psi$. (*a*) 3D visualization. (*b*) 2D visualization on a ϕ–θ plane. The position of the FILD detectors is indicated in (*b*).

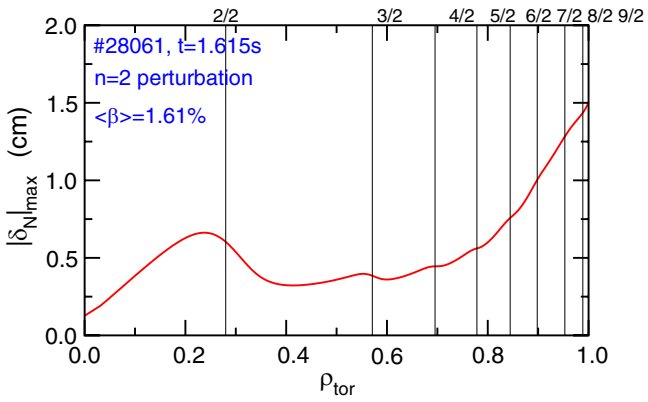

Figure 12. NEMEC. Maximum corrugation $|\delta_N|_{max}$ as a function of ρ_{tor}.

implemented in M3D-C1 is described in detail in [14]. This model includes both the Hall term and electron gradient term in the generalized Ohm's law, and therefore self-consistently includes ion and electron diamagnetic drifts. These drifts are known to play an important role in the formation of islands due to applied non-axisymmetric fields [18]. The two-fluid terms in the M3D-C1 model enter with an ion-skin depth scaling. By artificially setting the value of the skin depth to zero, the one-fluid model is recovered [14]. In the one-fluid model, the electron and ion rotation frequencies are identical, and equal to the $E \times B$ frequency. The amplification of islands is typically not seen in the one-fluid model because the $E \times B$ frequency (and hence the electron rotation frequency) generally crosses zero either near the last closed flux surface (where the tearing

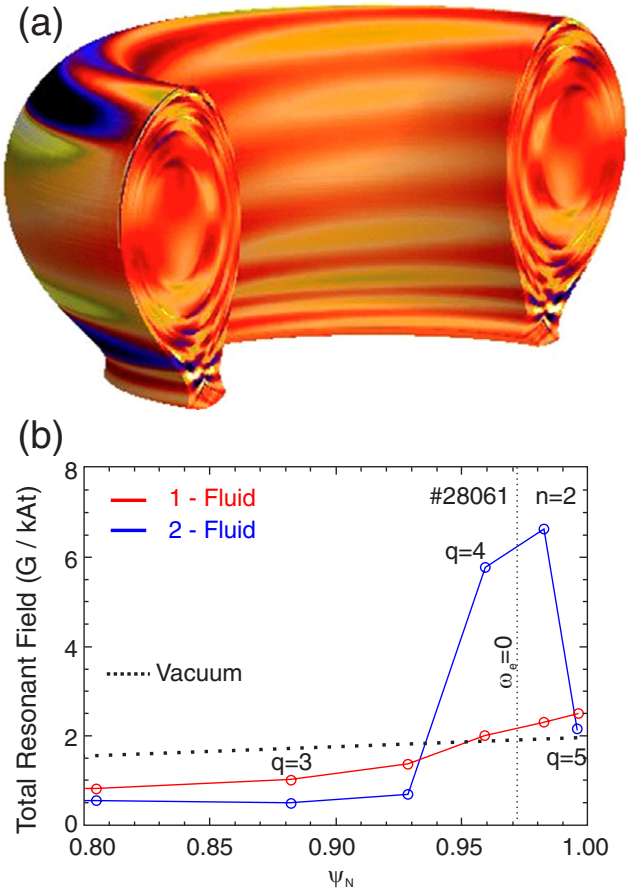

Figure 13. M3D-C1 simulation results of the $n = 2$ component of the perturbed radial magnetic field. (*a*) 3D view of the perturbed equilibrium. (*b*) Radial profiles of the total resonant components of the $n = 2$ harmonic calculated only in a vacuum (dashed line), and with the 1 (red) and 2 (blue) fluid models of the M3D-C1 code. Fluid simulations are shown at each rational $q = m/n$ surface, with straight lines connecting all radial locations.

drive is small due to low pressure and current density), or not at all. This is in contrast to the two-fluid case, where the electron diamagnetic term tends to cause the electron rotation to cross zero well within the plasma, where tearing modes are closer to marginal stability and hence easier to drive to finite amplitude. Figure 13 shows the M3D-C1 simulation results for this discharge at $t = 1.61$ s. The radial component of the perturbed magnetic field including plasma response is shown in figure 13(*a*) in a 3D view of the perturbed equilibrium. Figure 13(*b*) shows the total resonant field for the $n = 2$ component of the perturbation ac calculated using the vacuum field representation as well as the one- and two-fluids models of the M3D-C1 codes. The two-fluids model predicts a significant resonant field amplification at $\Psi_N \approx 0.96$ where the electron rotation is negligible. Only in that area are the 3D fields larger when including the plasma response than in the vacuum approach. In the plasma center, however, the perturbation is efficiently shielded and lies well below the vacuum field levels.

3.3. Orbit simulations

Three different models for the reconstruction of the 3D fields arising from the ELM mitigation coils, i.e., a vacuum, NEMEC

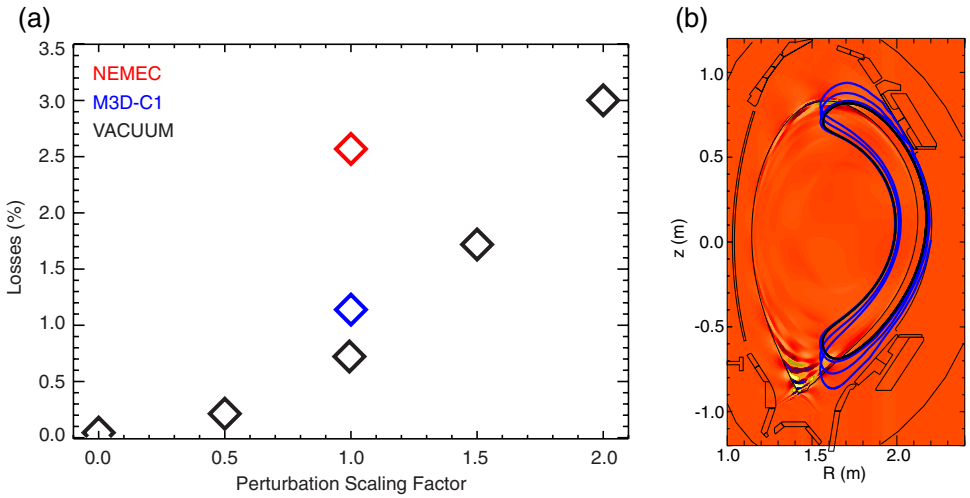

Figure 14. (*a*) Guiding center simulations of fast-ion orbits in 3D fields calculated using the 2 fluid M3D-C1 code, the free boundary NEMEC code and the 2D + 3D vacuum approach. (*b*) Typical perturbed banana orbit in M3D-C1 perturbed equilibrium.

and M3D-C1, have been used to calculate the fast-ion losses to the first wall using guiding center and full orbit simulations. The guiding center GOURDON code has been used to test the different models for the generation of the 3D fields with a simplified 3D wall and without collisions. A full orbit 3D simulation in vacuum fields with a realistic first wall and including collisions has been carried out with the ASCOT code. Figure 14(*a*), shows the final number of losses (as a % of total injected ions) as a function of the perturbation amplitude calculated using the vacuum approach (a scaling factor of 1 indicates the real experimental condition). The losses scale from almost zero for the 2D equilibrium (perturbation scaling factor $= 0$) up to $\approx$3.5% of the total injected ions when the 3D perturbation is doubled with a clear non-linear dependence on the scaling factor. The losses obtained using the NEMEC and M3D-C1 3D fields are also shown. At a realistic perturbation amplitude (scaling factor $= 1$), the highest losses are obtained using the NEMEC equilibrium (2.6%) while the lowest level of losses is obtained using the 3D fields calculated with the vacuum approach. The low level $\approx$1.2% of particle losses obtained using the M3D-C1 fields compared to the NEMEC fields could be due to the fact that M3D-C1 fields have been calculated only for the $n = 2$ component, though there are other important Fourier components in the perturbation spectra, e.g. $n = 6$, that could also lead to fast-ion transport. Another important difference could be that the TF ripple is included in the NEMEC simulations but not in the M3D-C1 and vacuum simulations (the lowest level of losses at realistic perturbation amplitudes). The perturbed trajectory of a banana orbit in a 3D M3D-C1 equilibrium is shown in figure 14(*b*) to illustrate the effect of the 3D fields on a typical banana orbit. It is worth noting that just a few bounces are enough to cause the loss of a trapped particle that would otherwise be well confined in the pedestal region. The heat loads on the first wall arising from the lost ions due to the 3D fields have been calculated using the full orbit GOURDON and ASCOT codes. GOURDON computes the heat loads on a 2D first wall using the NEMEC 3D fields (including TF ripple) without collisions. Figure 15 shows the heat load calculated by GOURDON on

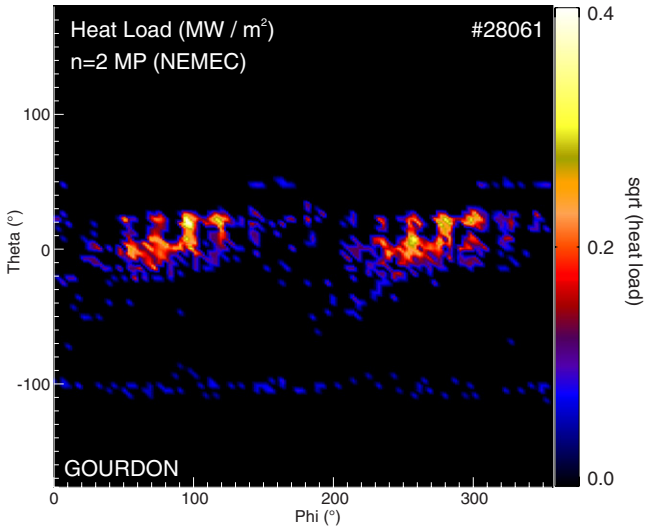

Figure 15. GOURDON simulations. Fast-ion heat load on a 2D AUG first wall computed with the full orbit GOURDON code in a NEMEC 3D equilibrium. The patterns of the $n = 2$ MP and of the TF ripple are clearly visible.

a ϕ–θ plane. The pattern of the TF ripple due to the 16 TF coils and of the $n = 2$ MP is clearly visible in the final heat loads. The ripple-induced losses are enhanced in the areas where the MPs are causing the losses ($n = 2$ pattern), indicating a synergistic effect between both 3D perturbations of the axialsymmetric equilibrium, though the peak heat loads are well below the measured levels. Fully 3D simulations (including a 3D first wall) have been carried out using the full orbit ASCOT code in vacuum fields. The simulated NBI wall loads for the two NBI beams (NBI#3 and NBI#8) are plotted in figure 16. Figure 16(*a*), without MPs, and (*b*), with MPs, show the wall loads on a 2D (ϕ–θ) plot with the position of the FILD detectors marked with red circles. Most of the particles end in the divertor in both cases while both FILD systems as well as the protruding limiters are getting significant heat loads in both cases. Note that the vertical heat load stripes correspond to protruding limiters and not to the TF ripple; this

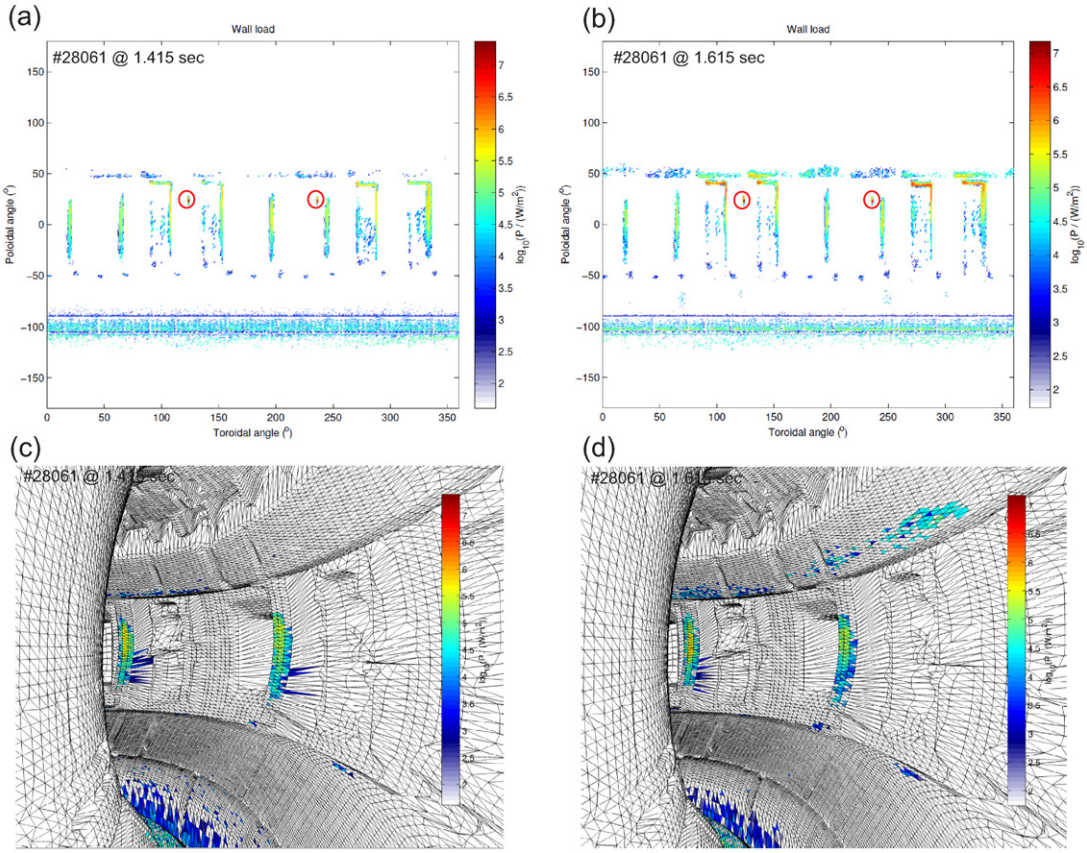

Figure 16. ASCOT simulations results of the fast-ion wall loads without, (*a*) and (*c*), and with, (*b*) and (*d*), MPs in 2D and 3D.

would exhibit the 16 vertical stripes (due to the 16 TF coils) of figure 15. New wall areas around the PSL are clearly loaded with impacts of escaping particles when the coils are switched ON. Although the 3D wall structure may blur the effect, the pattern of the $n = 2$ perturbation is still clearly visible on the wall load at a poloidal angle of $\approx 50^{\circ}$. ASCOT simulations clearly overestimate the fast-ion losses using vacuum fields as they predict $\approx 15\%$ of injected particle losses and a heat load of $\approx 7\,\mathrm{MW\,m^{-2}}$ on the FILD detector head, while infra-red measurements give a maximum of $2.2\,\mathrm{MW\,m^{-2}}$ due to the externally applied MPs on protruding tiles.

4. Summary and conclusions

A strong interaction between fast-ions, and spontaneous (ELMs) and externally applied edge perturbations, has been observed in the AUG tokamak. Multiple filament-like bursts of fast-ion losses are observed during ELMs by FILD detectors located at different positions. Externally applied MPs have little effect on plasma profiles, including fast-ions, in high collisionality plasmas with mitigated ELMs. A strong impact on plasma density, rotation and fast-ions is observed, however, in low density/collisionality and low q_{95} plasmas with externally applied MPs and partially mitigated ELMs. The plasma response is dominated by a marginal ELM mitigation, a density pump out of up to 25% of the core line integrated signal and a clear plasma braking.

During the mitigation/suppression of type-I ELMs by externally applied MPs, the large fast-ion bursts observed during ELMs are replaced by a steady loss of fast-ions with a broad-band frequency and an amplitude of up to an order of magnitude higher than the NBI prompt loss signal without MPs. Beam ions with several pitch-angles and energies are detected during the MP phases though most of the ions are on banana orbits that explore the entire pedestal/scrape-off-layer (SOL). While ELM-induced fast-ion losses are typically observed by both detectors almost simultaneously, the 3D fields applied by the ELM mitigation coils concentrate the losses on FILD1, while FILD2 signals almost vanished highlighting the 3D character of the static low-n externally applied MP. The heat loads associated with the MP-induced fast-ion losses can be, in certain regions, up to six times larger than the measured heat loads without MPs with peak values $\approx 2.2\,\mathrm{MW\,m^{-2}}$. The lower density caused by the density pump-out during the MP phase leads to a lower collisionality that can explain the larger fast-ion content measured in the plasma with the FIDA diagnostic despite the strong losses measured with FILD and the infra-red camera. This lower density also leads to a deeper beam deposition with an inward radial displacement of ≈ 2 cm in the maximum of the BES emission.

Collisionless guiding center simulations of the measured fast-ion losses have been carried out using a 2D wall and the 3D fields calculated with the vacuum representation as well as with the M3D-C1 and NEMEC codes. At realistic perturbation

amplitudes (coil current), guiding center simulations using a 2D wall geometry predict losses that are ≈0.7%, ≈1.2% and ≈2.6% of the injected particles using the 3D fields calculated with the vacuum field representation, the M3D-C1 model and the NEMEC model respectively. Full orbit and guiding center simulations using the same 2D wall predict similar level of losses. On the contrary, collisional (including slowing down and pitch-angle scattering) full orbit simulations using a fully 3D wall with protruding tiles and vacuum fields clearly overestimate the number of particle losses with up to 15% of the injected particles and localized heat loads up to $7\,\mathrm{MW\,m^{-2}}$. A test of the different models for the 3D equilibrium reconstruction (including the coupling of several toroidal mode numbers) will be done in the future using full orbit 3D simulations and taking into account slowing down and pitch-angle scattering.

Acknowledgments

This research was supported in part by the Spanish Ministry of Economy and Competitiveness (RYC-2011-09152 and ENE2012-31087) and a Marie Curie FP7 Integration Grant (PCIG11-GA-2012-321455).

References

[1] Hender T C *et al* 1992 Effect of resonant magnetic perturbations on compass-c tokamak discharges *Nucl. Fusion* **32** 2091
[2] Evans T E *et al* 2004 Suppression of large edge-localized modes in high-confinement diii-d plasmas with a stochastic magnetic boundary *Phys. Rev. Lett.* **92** 235003
[3] Liang Y *et al* 2007 Active control of type-i edge-localized modes with $n = 1$ perturbation fields in the jet tokamak *Phys. Rev. Lett.* **98** 265004
[4] Suttrop W *et al* 2011 First observation of edge localized modes mitigation with resonant and nonresonant magnetic perturbations in ASDEX Upgrade *Phys. Rev. Lett.* **106** 225004
[5] Shinohara K *et al* and the ITPA Topical Group on Energetic Particles 2011 *Nucl. Fusion* **51** 063028
[6] Spong D A 2011 *Phys. Plasmas* **18** 056109
[7] Heyn M F, Ivanov I B, Kasilov S V, Kernbichler W, Loarte A, Nemov V V and Runov A M 2012 *Nucl. Fusion* **52** 054010
[8] Koskela T, Asunta O, Hirvijoki E, Kurki-Suonio T and Akaslompolo S 2012 *Plasma Phys. Control. Fusion* **54** 105008
[9] Tani K, Shinohara K, Oikawa T, Tsutsui H, Miyamoto S, Kusama Y and Sugie T 2012 *Nucl. Fusion* **52** 013012
[10] Garcia-Munoz M, Fahrbach H-F, Pinches S D, Bobkov V, Bruedgam M and Gobbin M 2009 Mhd induced fast-ion losses in the ASDEX Upgrade tokamak *Nucl. Fusion* **49** 085014
[11] Hirshman S, van Rij W I and Merkel P 1986 *Comput. Phys. Commun.* **43** 143
[12] Strumberger E, Guenter S and Tichmann C 2013 *Nucl. Fusion* submitted
[13] Ferraro N M and Jardin S C 2009 *J. Comp. Phys.* **228** 7742
[14] Ferraro N M 2012 *Phys. Plasmas* **19** 056105
[15] Geiger B, Garcia-Munoz M, Heidbrink W W, McDermott R M, Tardini G, Dux R, Fischer R, Igochine V and the ASDEX Upgrade Team 2011 Fast-ion D-alpha measurements at ASDEX Upgrade *Plasma Phys. Control. Fusion* **53** 065010
[16] Fundamenski W, Naulin V, Neukirch T, Garcia O E and Rasmussen J J 2007 On the relationship between elm filaments and solar flares *Plasma Phys. Control. Fusion* **49** R43
[17] Viezzer E, Puetterich T, Dux R, McDermott R M and the ASDEX Upgrade Team 2012 High-resolution charge exchange measurements at ASDEX Upgrade *Rev. Sci. Instrum.* **83** 103501
[18] Fitzpatrick R and Hender T C 1991 *Phys. Fluids* B **3** 644